Chemical Engineering Science 284 (2024) 119473

Contents lists available at ScienceDirect

Chemical Engineering Science

journal homepage: www.elsevier.com/locate/ces

Modeling of a catalytic fluidized bed reactor via coupled CFD-DEM with MGM: From intra-particle scale to reactor scale

M. Hadian [a], M.J.A. de Munck [a], K.A. Buist [a,*], A.N.R. Bos [b,c], J.A.M. Kuipers [a]

[a] Multiphase Reactors Group, Department of Chemical Engineering & Chemistry, Eindhoven University of Technology, P.O. Box 513, 5600 MB Eindhoven, the Netherlands

[b] Shell Global Solutions International B.V., P.O. Box 38000, 1030 BN Amsterdam, Netherlands

[c] Laboratory for Chemical Technology, Ghent University, Technologiepark 125, Ghent 9052, Belgium

ABSTRACT

The Computational Fluid Dynamics - Discrete Element Method (CFD-DEM) method is extended by coupling with the multi-grain model (MGM) to include particle growth due to a gas-solid reaction, as well as intra- and inter-particle phenomena such as heat and mass transfer, and reaction, next to the inter-particle and fluid-particle interactions in the reactor. This comprehensive model treats each particle individually and accounts for changes in particle properties due to both the particle growth and temporal and spatial variations of the process conditions. It also captures the impact of the change in the particles' properties on the fluidized bed reactor characteristics, such as the hydrodynamic regime. The results of the model revealed that the fluidization characteristics and solids mixing can be altered by particle growth. Particle growth also led to the formation of a particle size gradient along the height of the reactor. The coupling allows for monitoring of both external and internal mass transfer limitations. For the adopted reaction kinetics, growth rate and properties the external mass transfer limitations remained negligible, however the internal mass transfer limitation plays a significant role in the process performance.

1. Introduction

Many chemical processes such as polymerization, oxidative coupling of methane, and ThermoCatalytic Decomposition of methane (TCD), utilize catalytic fluidized bed reactors. In a catalytic fluidized bed, the scale of the effective phenomena can vary from the mass and heat transfer within the micro-scale of a porous particle, to the interaction of particles with each other and the fluid phase and the scale of the reactor when it comes to solids circulation patterns. Modeling these multi-phase phenomena is crucial in developing and optimizing the process. Numerical simulations with multi-scale models enable engineers to investigate multiphase flows in industrial chemical processes.

Computational Fluid Dynamics – Discrete Element Method (CFD-DEM) is known as a multi-scale Eulerian-Lagrangian technique to simulate processes involving fluid and solid particles (Tsuji et al., 1993; De Jong et al., 2012; Golshan et al., 2020; Mu et al., 2020; Norouzi et al., 2016). CFD-DEM is a powerful method to model systems that include multi-scale solid-fluid interactions such as encountered in fluidized beds, spouted beds and pneumatic conveyors. Although CFD-DEM covers a wide range of the mentioned scales and can include heat and mass transfer between the continuous and discrete phases, it mostly assumes uniform (lumped) conditions inside the particles ($Bi \leq 0.1$) for both heat and mass and it lacks the intra-particle phenomena (Golshan et al., 2020; Finotello et al., 2019; Zhuang et al., 2014; Lu et al., 2020). In some processes, such as polymerization or TCD, catalyst particles grow in size over time and therefore the Biot number changes over time and in general also in space, and from particle to particle.

Several publications have explored the use of CFD-DEM models in conjunction with intra-particle models to investigate biomass pyrolysis in FBR. Wang et al. have extended the CFD-DEM model by incorporating a 1D thermally thick model to capture internal heat transfer and heat of reaction (Wang et al., 2022). Oyedeji et al. have employed a CFD-DEM model coupled with a 2D model to simulate cylindrical biomass particles (Oyedeji et al., 2022; Pecha et al., 2021). In another study, the impact of biomass shape was investigated using a 3D glued-spheres particle model (Lu et al., 2021). While these 2D and Shape dependent models offer valuable insights for fundamental research, they can be computationally expensive. Furthermore, none of these models account for the influence of intra-particle reactions and the subsequent particle growth on FBR hydrodynamics.

In an earlier contribution, the authors developed the Multi-Grain Model (MGM) that models the particle growth, by combining the surface reaction and deactivation kinetics, as well as intra-particle heat and mass transfer of reactants and products (Hadian et al., 2021). MGM

* Corresponding author.
E-mail address: k.a.buist@tue.nl (K.A. Buist).

https://doi.org/10.1016/j.ces.2023.119473
Received 25 August 2023; Received in revised form 18 October 2023; Accepted 3 November 2023
Available online 15 November 2023

Nomenclature

A	Heat or mass exchange area (m^2)
A_c	Cross section area of the reactor (m^2)
a_d	Exchange surface area per unit length of the reactor (m^2/m)
CF	Reaction rate unit conversion factor ($kg_{reactant} \cdot g_{cat}/mol_{reactant}/m^2_{cat}$)
Cp	Specific heat capacity ($J/K/kg$)
$\mathcal{D}_f$, D	Diffusivity (m^2/s)
$D(\mathbf{r}-\mathbf{r}_{\mathbf{p,a}})$	Distribution function (-)
$\langle d \rangle$	Sauter mean diameter (m)
dt	time step size (s)
h	Heat transfer coefficient ($W/m^2/K$)
$\mathbf{I}$	Unity tensor (-)
I	Moment of inertia ($kg \cdot m^2$)
k_m	Mass transfer coefficient (m/s)
K	Thermal conductivity in the gas phase ($W/m/K$)
k	Thermal conductivity in the porous particle ($W/m/K$)
$\hat{k}_1$	Reaction rate constant of pseudo-first-order reaction ($1/s$)
M	Mass concentration (kg/m^3)
m	mass (kg)
MW	Molar mass (kg/mol)
N	Number of particles (-)
n_p	number of particles per unit height of the reactor (-)
P	Pressure (Pa)
Q_p	Energy source term in the cell (W/m^3)
q_p	Heat transfer of particle (W)
$r(t)$	Actual reaction rate ($mol_{reactant}/g_{cat}/s$)
$r'(t)$	Pseudo-first-order reaction rate ($mol_{reactant}/m^3/s$)
r	Radial position in the particle (m)
$\mathbf{r}_{p,a}$	Position vector of particle a in reactor (m)
r_g	Radial position in the grain (m)
$r_{g,p}$	Position of the grain in the particle (m)
$R(r,t)$	Volumetric average rate of reaction ($kg/m^3/s$)
S_m	Mass source term in the cell ($kg/m^3_{cell}/s$)
$\mathbf{S}_p$	Momentum Source term in the cell ($kg \cdot m/m^3/s^2$)
t	time (s)
T	Temperature (K)
$\mathbf{T}$	Torque ($kg \cdot m^2/s^2$)
$\mathbf{u_f}$	Fluid velocity vector (m/s)
$\mathbf{v_p}$	Particle velocity vector (m/s)
V	Volume (m^3)
w	Rotational velocity ($1/s$)
Bi	Biot number (-)
Nu	Nusselt number (-)
Pr	Prandtl number (-)
Re	Reynolds number (-)
Sh	Sherwood number (-)
Sc	Schmidt number (-)
β	Inter-phase friction coefficient (-)
ε	Gas volume fraction (m^3_{gas}/m^3_{cell})
ρ	Density (kg/m^3)
μ	Shear viscosity ($Pa \cdot s$)
τ	Viscous stress tensor (Pa)
θ	Dimensionless temperature (-)
Ψ	Mass source term of each particle ($kg/m^3/s$)

Subscripts and Superscripts

f	Fluid
p	Particle
a	DEM particle a
i	Component i
in	Inlet
mix	Gas mixture
g	Grain in MGM
eff	Effective
$bulk$	Local conditions in the gas phase
s	Particle's surface conditions
$cell$	CFD computational grid cell
$prod$	Solid product layer in grains of MGM

provides insight into the importance of effective phenomena in an isolated particle and the change of particle parameters such as size and density (Chiovetta and Estenoz, 2004; McKenna and Soares, 2001; Hadian et al., 2021). However, it does not include the consequence of this evolution on the reactor characteristics, such as the hydrodynamics of the bed.

The particle properties and the overall reactor conditions as well as local conditions can significantly affect each other (Li et al., 2017). Therefore, coupling CFD-DEM with MGM combines the potential of both approaches and allows us to capture the effects of dynamic catalyst characteristics on the reactor conditions and vice versa. One example is the influence of the increased particle size and mass on the fluidized bed hydrodynamics. Besides, it is possible to study the temperature and concentration profiles and their importance in the reactor. As a result, the combined CFD-DEM-MGM methodology produces a more comprehensive representation of reality and is expected to produce more accurate results. This model enables engineers to predict the reactor performance over time and optimize the design and conditions of the reactor for industrial processes such as TCD and polyolefins production.

The outline of this article is as follows: in section 2 the coupled CFD-DEM-MGM model and the implementation of the coupling are described. In section 3 the implementation of the method is verified using analytical solutions. The results and discussion are presented in section 4. Finally in section 5 the conclusions are presented.

2. Model description

CFD-DEM-MGM consists of three sub-models that are coupled with each other. CFD is responsible for modeling the continuous (gas) phase, including the momentum, energy and mass of species balances. DEM models the interaction of the particles with the gas phase; heat and mass transfer and drag and the interactions of the particles with each other and the reactor walls; collisions. MGM handles the heat and mass balance at the smallest scale: the reaction and mass deposition inside each of the particles individually.

2.1. Gas phase modeling

The gas phase is described by the volume-averaged Navier-Stokes equation (1) and the continuity equation (2) (Anderson and Wendt, 1995):

$$\frac{\partial(\varepsilon_f \rho_f \mathbf{u}_f)}{\partial t} + \nabla \cdot (\varepsilon_f \rho_f \mathbf{u}_f \mathbf{u}_f) = -\varepsilon_f \nabla P_f - \nabla \cdot (\varepsilon_f \tau_f) + \varepsilon_f \rho_f \mathbf{g} - \mathbf{S}_p \quad (1)$$

$$\frac{\partial(\varepsilon_f \rho_f)}{\partial t} + \nabla \cdot (\varepsilon_f \rho_f \mathbf{u}_f) = \sum_{i=1}^{n_c} S_{m,i} \quad (2)$$

In all equations, the subscript f indicates the fluid phase and p the particulate phase. ε is the gas volume fraction in the cell, ρ the density, $\mathbf{u_f}$ the fluid velocity and P_f the pressure. τ_f is the gas phase viscous stress tensor, provided by equation (3), which is assumed to follow the general Newtonian form (Anderson and Wendt, 1995):

$$\tau_f = -\mu_f \left[(\nabla \mathbf{u}_f) + (\nabla \mathbf{u}_f)^T - \frac{2}{3}(\nabla \cdot \mathbf{u}_f)\mathbf{I} \right] \tag{3}$$

where μ_f is the shear viscosity, and $\mathbf{I}$ the unity tensor. $S_{m,i}$ is the mass source of component i in the cell and is detailed in section 2.2.1. The fluid is assumed to be gas, thus the fluid density, ρ_f is dependent on the gas composition and is calculated according to the ideal gas law, equations (4) and (5) respectively.

$$MW_{mix} = \sum_{i=1}^{n_c} y_i MW_i \tag{4}$$

$$\rho_f = \frac{P\, MW_{mix}}{R T_f} \tag{5}$$

where y_i the mole fraction of component i, MW_i and MW_{mix} are the molar mass of component i and the mixture.

$\mathbf{S}_p$ in equation (1) is the source term accounting for coupling of momentum exchange between the fluid and the particles given by equation (6) (Patil et al., 2015):

$$\mathbf{S_p} = \frac{1}{V_{cell}} \sum_{a=0}^{N_p} \frac{V_{p,a}\beta_a}{1-\varepsilon_f} (\mathbf{u}_f - \mathbf{v}_{p,a}) D(\mathbf{r} - \mathbf{r}_{p,a}) \tag{6}$$

where V_{cell} and $V_{p,a}$ represent the local cell volume and the volume of particle a. Due to the growing nature of particles, the poly-disperse drag correlations proposed by Sarkar and Beetstra (Sarkar et al., 2009; Beetstra et al., 2007), equations (7) and (8) are used to calculate the interface momentum exchange coefficient, β. The distribution function, D, ensures that the drag force acts as a point force at the center of mass of the particle (Patil et al., 2015). The mapping of local properties from Eulerian grid to Lagrangian particle positions and vice versa is performed by using a volume-weighing techniques developed by Hoomans et al. (1996).

$$\beta_a = \left[\frac{d_{p,a}}{\langle d \rangle} + 0.064 \left(\frac{d_{p,a}}{\langle d \rangle} \right)^3 \right] \beta_{mono}(\varepsilon_f, \langle \mathrm{Re} \rangle) \tag{7}$$

$$\beta_{mono}(\varepsilon_f, \langle \mathrm{Re} \rangle) = 180 \frac{\mu_g (1-\varepsilon_f)^2}{\langle d \rangle^2 \varepsilon_f} + 18 \frac{\mu_g \varepsilon_f^3 (1-\varepsilon_f)(1+1.5\sqrt{(1-\varepsilon_f)})}{d_p^2} + 0.31 \frac{\mu_g (1-\varepsilon_f)\langle \mathrm{Re} \rangle}{\langle d \rangle^2 \varepsilon_f} \left[\frac{\varepsilon_f^{-1} + 3\varepsilon_f(1-\varepsilon_f) + 8.4\langle \mathrm{Re} \rangle^{-0.343}}{1 + 10^{3(1-\varepsilon_f)} \mathrm{Re}^{-2.5+2\varepsilon_f}} \right] \tag{8}$$

Where $\langle Re \rangle$ is the average Reynolds number in the cell, equation (9), calculated by the Sauter mean diameter, equation (10).

$$\langle Re \rangle = \frac{\varepsilon_f \rho_f (|\mathbf{u}_f - \mathbf{v}_{p,a}|) \langle d \rangle}{\mu_f} \tag{9}$$

$$\langle d \rangle = \frac{\sum_{a=1}^{N_{cell}} d_{p,a}^3}{\sum_{a=1}^{N_{cell}} d_{p,a}^2} \tag{10}$$

with N_{cell} indicating the total number of particles in the computational cell and $\mathbf{v}_{p,a}$ is the velocity particle a.

The gas phase thermal energy balance is given by equation (11) (Finotello et al., 2019):

$$Cp_f \left[\frac{\partial(\varepsilon_f \rho_f T_f)}{\partial t} + \nabla \cdot (\varepsilon_f \rho_f \mathbf{u}_f T_f) \right] = \nabla \cdot (\varepsilon_f K_f^{\mathrm{eff}} \nabla T) + Q_p \tag{11}$$

T is temperature, and Q_p represents the energy source term originating from the energy transport between the fluid and the particulates detailed in section 2.2.1. K_f^{eff} is the effective thermal conductivity of the fluid, that is calculated from the thermal conductivity of the fluid, K_f, and the fluid volume fraction, ε_f, via equation (12):

$$K_f^{\mathrm{eff}} = \frac{1-\sqrt{1-\varepsilon_f}}{\varepsilon_f} K_f \tag{12}$$

The component mass balance is described by equation (13) considering convection, diffusion and a source term due to mass exchange with the catalyst particles (Wendt et al., 2009; Finotello et al., 2019):

$$\frac{\partial(\varepsilon_f M_{f,i})}{\partial t} + \nabla \cdot (\varepsilon_f M_{f,i} \mathbf{u_f}) = \nabla \cdot (\varepsilon_f D_{f,i}^{\mathrm{eff}} \nabla M_{f,i}) + S_{m,i} \tag{13}$$

where $M_{f,i}$ is the mass concentration of components in the fluid, and the effective diffusivity of component i in the fluid, $D_{f,i}^{\mathrm{eff}}$, is calculated in a similar fashion as K_f^{eff}, using equation (14). $S_{m,i}$ is the gas-particle mass source term transfer of component i and is defined in section 2.2.2

$$D_{f,i}^{\mathrm{eff}} = \frac{1-\sqrt{1-\varepsilon_f}}{\varepsilon_f} D_{fi} \tag{14}$$

The flow field governing equations are solved via Projection method, while Dirichlet boundary condition is used for the inlet of the gas phase, and a fixed pressure boundary condition of 1 atm at the top of the domain was applied. The side boundary conditions are considered walls with no-slip conditions.

2.2. Discrete phase modeling

2.2.1. DEM

The trajectory of individual particles in DEM are tracked by Newton's second law of motion, equation (15). Forces acting on the particle are on the right-hand side. These forces include the pressure gradient force, drag force, gravitational force and collisional forces, respectively. The particle-particle and particle-wall collisions are described by the soft-sphere model developed by Cundall and Strack (1979). In this approach, the contact forces are calculated using a linear spring and dashpot model (Patil et al., 2015; Buist et al., 2016; Kloss et al., 2012).

$$m_{p,a} \frac{d\mathbf{v}_{p,a}}{dt} = m_{p,a} \frac{d^2 \mathbf{r}_{p,a}}{dt^2} = -V_{p,a} \nabla P_f + \frac{V_{p,a}\beta_{p,a}}{1-\varepsilon_f} (\mathbf{u}_f - \mathbf{v}_{p,a}) + m_{p,a}\mathbf{g} + \sum \mathbf{F}_{contact,p,a} \tag{15}$$

in which $\mathbf{r}_{p,a}$ and $m_{p,a}$ are the position and the mass of the particle a.

Rotational motion of the particle is computed using equation (16).

$$I_{p,a} \frac{d\mathbf{w}_{p,a}}{dt} = \mathbf{T}_{p,a} = \sum_{\mathrm{b} \in \text{contact list}} (r_{p,a} \mathbf{n}_{ab} \times \mathbf{F}_{ab,t}) \tag{16}$$

where $I_{p,a}$ is the moment of inertia, $\mathbf{w_{p,a}}$ is the rotational velocity and $\mathbf{T}_{p,a}$ is the torque.

The mass and heat transfer between the fluid and particles is performed in 7 steps as shown in Fig. 1. In each time step, the local fluid temperature and concentration at the particle position is obtained. The local gas-particle heat and mass transfer coefficients are calculated. These transfer coefficients are used in the multi-grain model. The calculation of the particle surface temperature and concentrations is described in section 2.2.2. DEM obtains the particle temperature and concentration surface values from MGM and calculates the heat and mass transfer rates between particles and the fluid. In the last step, these transfer rates are coupled back to the Eulerian grid cells and are used as source terms in the gas thermal energy and mass balances, shown in equations (11) and (13) respectively.

The energy source term, Q_p in equation (11) is calculated from:

$$Q_p = \frac{1}{V_{cell}} \sum_{a=0}^{N_p} h_{p,a} A_{p,a} (T_{p,a} - T_f) D(\mathbf{r} - \mathbf{r_{p,a}}) \tag{17}$$

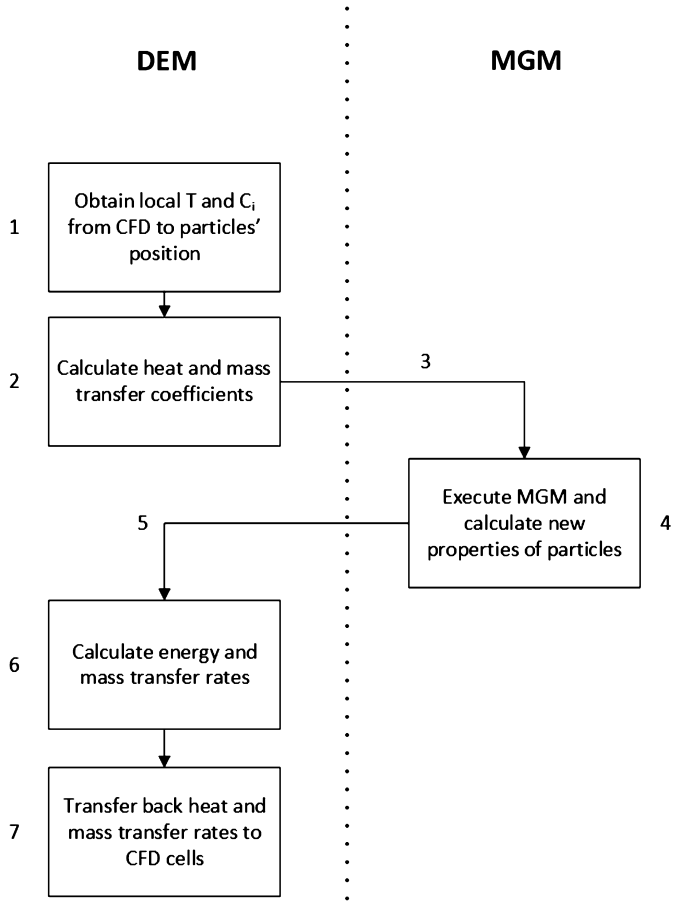

Fig. 1. Schematic diagram of heat and mass transfer coupling steps between fluid and particles.

where $A_{p,a}$ is the heat exchanging surface area of particle a, and h_a the heat transfer coefficient calculated using the Nusselt number, Nu, from the Gunn correlation, equation (18) (Gunn, 1978):

$$Nu = \frac{h_a d_{p,a}}{k_f} = (7 - 10\varepsilon_f + 5\varepsilon_f^2)(1 + 0.7Re^{0.2}Pr^{0.33}) + (1.33 - 2.4\varepsilon_f + 1.2\varepsilon_f^2)Re^{0.7}Pr^{0.33} \quad (18)$$

Re and Pr are Reynolds and Prandtl number respectively:

$$Re = \frac{\varepsilon_f \rho_f (|\mathbf{u}_f - \mathbf{v}_p|) d_{p,a}}{\mu_f} \quad (19)$$

$$Pr = \frac{\mu_f Cp_f}{K_f} \quad (20)$$

The mass source term of component i in equation (13) and in the continuity equation (2), $S_{m,i}$, is calculated from equation (21).

$$S_{m,i} = \frac{1}{V_{cell}} \sum_{a=0}^{N_p} k_{m,a,i} A_{p,a} (M_{p,a} - M_i) D(\mathbf{r} - \mathbf{r_{p,a}}) \quad (21)$$

where the mass transfer coefficient of component i between particle a and the fluid, $k_{m,a,i}$, is determined by the Sherwood number. The Sherwood number is computed using the Gunn correlation for mass transfer, equation (22). Sc is the Schmidt number, calculated from equation (23) (Gunn, 1978).

$$Sh_i = \frac{k_{m,a,i} d_{p,a}}{D_{f,i}} = (7 - 10\varepsilon_f + 5\varepsilon_f^2)(1 + 0.7Re^{0.2}Sc^{0.33}) + (1.33 - 2.4\varepsilon_f + 1.2\varepsilon_f^2)Re^{0.7}Sc^{0.33} \quad (22)$$

$$Sc = \frac{\mu_f}{\rho_f D_{f,i}^{\text{eff}}} \quad (23)$$

2.2.2. MGM

Each individual particle is modeled as a porous medium by MGM. In this model, the catalyst support is assumed to consist of several layers of solid spheres, called grains, with uniform coverage of active material on their surfaces, Fig. 2. Heat and mass transfer is considered in the radial direction at two different scales and the reaction occurs at the surface of the grains. At the macro particle scale the component concentrations and temperature are governed by via equations (24) and (25):

$$\frac{\partial M_{p,a,i}(r,t)}{\partial t} = \frac{1}{r^2}\frac{\partial}{\partial r}\left(D_{p,a,i}^{\text{eff}} r^2 \frac{\partial M_{p,a,i}(r,t)}{\partial r}\right) - R(r,t) \quad (24)$$

$$\frac{\partial T_{p,a}(r,t)}{\partial t} = \frac{1}{r^2}\frac{\partial}{\partial r}\left(\frac{k_{p,a}^{\text{eff}}}{\rho_p Cp_p} r^2 \frac{\partial T_{p,a}(r,t)}{\partial r}\right) - \frac{\Delta H}{\rho_p Cp_p} R(r,t) \quad (25)$$

where r is the radial position in particle and $D_{p,a,i}^{\text{eff}}$ the effective diffusivity of component i, $k_{p,a}^{\text{eff}}$, ρ_p and Cp_p the heat conductivity, the density and the specific heat capacity of the particle respectively, and $R(r,t)$ the volumetric average rate of reaction at a given radial position.

The concentration and temperature at the grain scale is also modeled by equations (26) and (27). The reaction occurs at the surface of the core of these grains and therefore appears in the boundary conditions, equation (28). The solid product of the reaction accumulates on the grains' surface causing an increase in radius leading to the alteration of the inter-particle diffusion limitation.

$$\frac{\partial M(r_g,t)}{\partial t} = \frac{1}{r_g^2}\frac{\partial}{\partial r_g}\left(D_{prod} r_g^2 \frac{\partial M(r_g,t)}{\partial r_g}\right) \quad (26)$$

$$\frac{\partial T(r_g,t)}{\partial t} = \frac{1}{r_g^2}\frac{\partial}{\partial r_g}\left(\frac{k_g}{\rho_{gr} C_{P_g}} r_g^2 \frac{\partial T(r_g,t)}{\partial r_g}\right) \quad (27)$$

$$D_{prod}\frac{\partial M(R_{g0},t)}{\partial r_g} = r(t).CF \quad (28)$$

where r_g is the radial position in the grain, D_{prod} is the effective diffusivity in the product layer around the grains, R_g is the radius of the whole-grain and $r_{g,p}$ is the position of the grain in the particle (Fig. 2) and CF is the unit conversion factor. For further details on MGM and its implementation and verification we refer to Hadian et al. (2021).

Intra-particle mass and heat balance are coupled with the fluid as explained in section 2.2.1 by continuous flux as the boundary conditions on the surface of the particle, equations (29) and (30):

$$B.C.@r = R_p \quad -D_{p,a,i}^{\text{eff}}\frac{\partial M_{p,a,i}}{\partial r} = k_{m,a,i}\left(M_{p,a,i} - M_{f,i}\right) \quad (29)$$

$$B.C.@r = R_p \quad -k_{p,a}^{\text{eff}}\frac{\partial T_p}{\partial r} = h_a\left(T_p - T_f\right) \quad (30)$$

3. Verification of the model

The implementation of the model is verified by comparing the results with analytical solutions in specific cases. Two-way heat and mass transfer between fluid and particles, the effect of removed mass from fluid to the particle on the fluid velocity, and the total mass balance of the reactor are evaluated and verified in the sections 3.1 to 3.4.

3.1. Temperature coupling

The heat transfer coefficient for each individual particle is calculated from equation (18). Assuming a lumped particle temperature ($Bi_p << 1$), the gas-particle heat transfer and the subsequent particle temperature change are calculated by the equations (31) and (32) respectively.

$$q_p = h(4\pi r_p^2)(T_p - T_f) \quad (31)$$

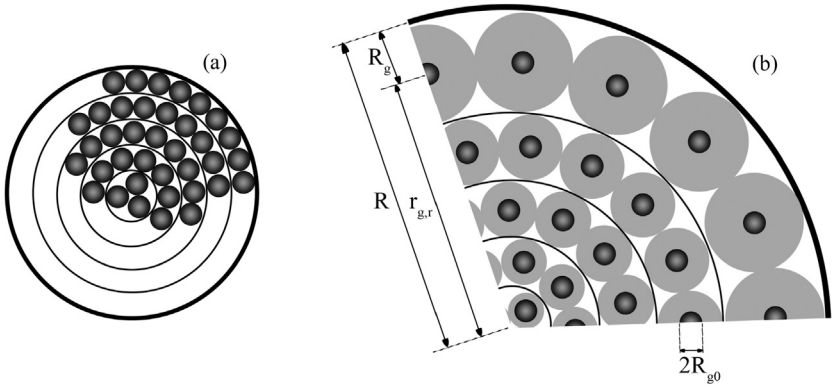

Fig. 2. Schematic of MGM model and layers of grains. (a) The particle before solid formation and growth. (b) A circular sector of the particle with the accumulated solid product on the surface of grains (Hadian et al., 2021).

Table 1
Simulation settings and properties of the verification cases.

Parameter	Single particle case	Packed bed case	Unit
Reactor dimensions (width×depth×height)	$0.1 \times 0.1 \times 0.1$	$0.03 \times 0.03 \times 0.2$	m
Field grid size	$10 \times 10 \times 10$	$10 \times 10 \times 80$	-
Flow time step size	5×10^{-4}	5×10^{-4}	s
Particle time step size	1×10^{-4}	1×10^{-4}	s
Number of particles	1	135000	-
Particles diameter	0.4	1	mm

$$\frac{dT_p}{dt_{DEM}} = -\frac{q_p}{V_p \rho_p C p_p} \tag{32}$$

In order to verify the implementation of the heat transfer, two tests were performed. In the first test a single particle ($T_{p,0} = 350\,°C$) is placed in a fluid with constant temperature ($T_f = 400\,°C$), Fig. 3-left. The heat transfer coefficient is constant and calculated according to terminal particle velocity. The particle temperature over time can then be calculated by equation (33), obtained from the analytical solution. Table 1 presents other simulation parameters.

$$\frac{T_{p,t} - T_f}{T_{p,0} - T_f} = exp\left(\frac{-h(4\pi r_p^2)t}{V_p \rho_p C p_p}\right) \tag{33}$$

Fig. 4 compares the simulation results with the analytical solution. A perfect match of the temperature of the DEM object verifies the CFD to DEM heat transfer implementation.

In the second test case, the two-way gas-particle heat transfer is verified using a packed bed of $(30 \times 30 \times 150)$ particles with initial temperature of 300 °C, Fig. 3-right. The initial gas phase temperature is also equal to 300 °C. At time $t = 0$ s, a fluid flow with a temperature (400 °C) enters from the bottom of the bed, see Table 1 for other parameters. By applying a very high fluid Péclet number ($Pe = Re \times Pr$), the test case can be considered as a 1D convection problem. Equations (34) and (35) show the fluid and particle phase energy balances respectively at an axial position z in the bed.

$$\varepsilon_f \rho_f C p_f \frac{\partial T_{f,z}}{\partial t} = \varepsilon_f \rho_f C p_f u_{f,z} \frac{\partial T_{f,z}}{\partial t} - h A_p (T_{f,z} - T_{p,z}) \tag{34}$$

$$(1 - \varepsilon_f) \rho_p C p_p \frac{\partial T_{p,z}}{\partial t} = h A_p (T_{f,z} - T_{p,z}) \tag{35}$$

The details of the analytical solution for the temperature of the fluid over time can be found in the references Anzelius (1926); Bateman (1932); Hougen et al. (1947); Bird et al. (2001). Fig. 5 illustrates the dimensionless temperature (equation (36)) along the height of the bed at different times. From this figure, it is evident that there is a good agreement between the analytical solution and the simulation results, which supports that the two-way gas-particle heat transfer coupling is correctly implemented.

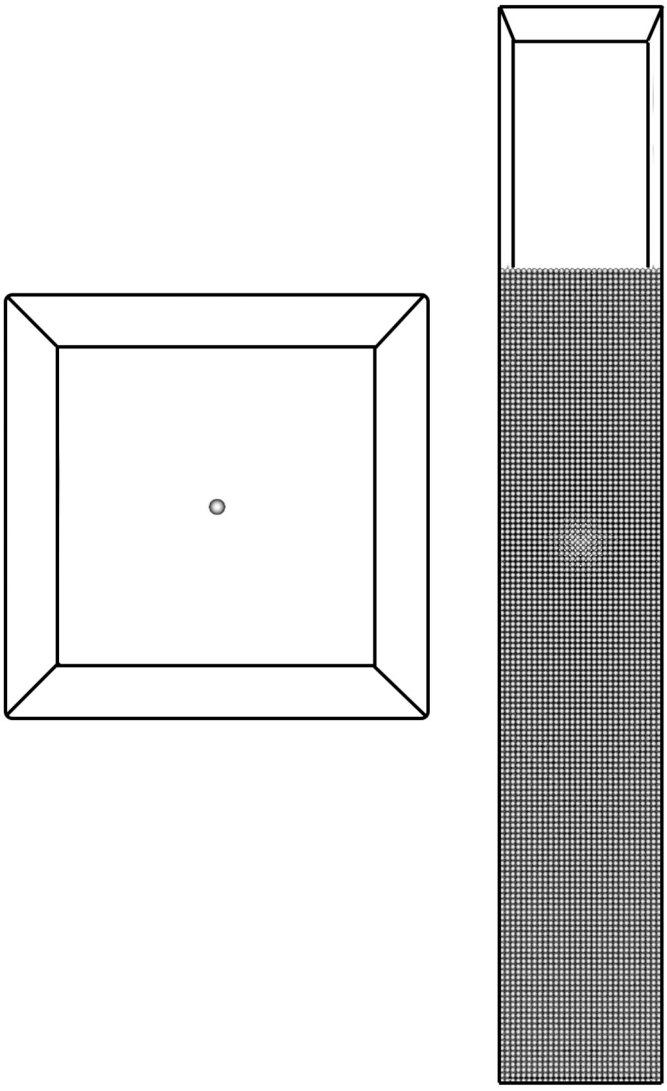

Fig. 3. The test case of verification of one-way heat and mass transfer (left) and two-way heat and mass transfer (right).

$$\theta = \frac{T_f - T_0}{T_{in} - T_0} \tag{36}$$

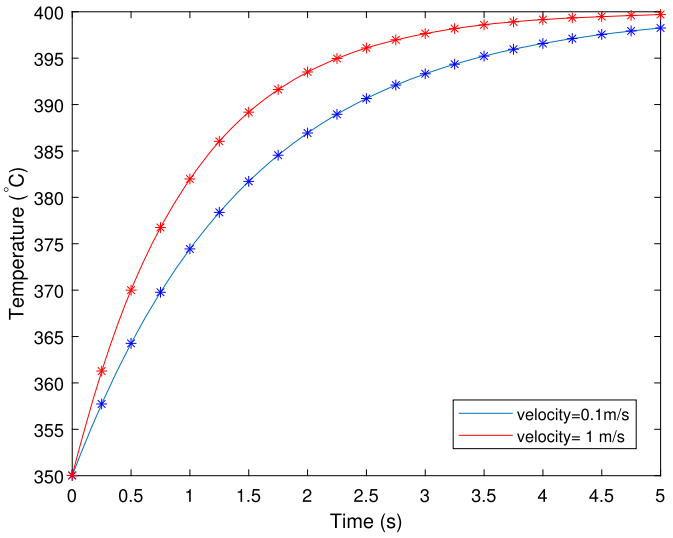

Fig. 4. Verification of the fluid to particle heat transfer with varying the falling particle velocity. Lines: analytical solutions. Symbols: simulation results.

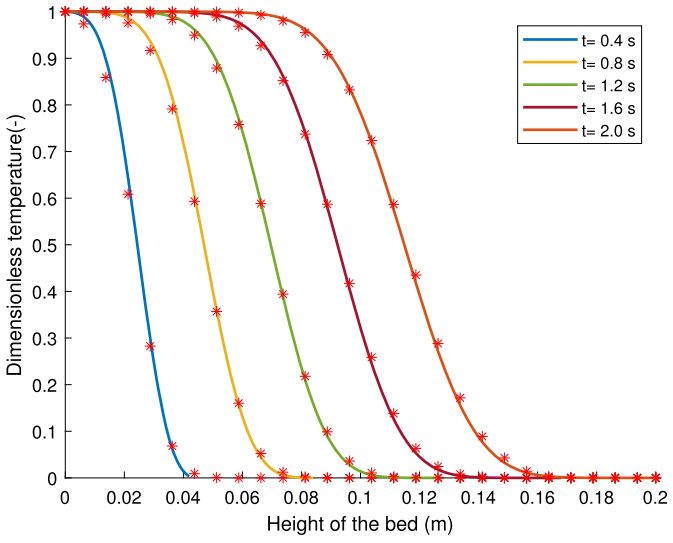

Fig. 5. Verification of the two-way heat transfer between CFD and DEM. Lines: analytical solutions. Symbols: simulation results.

3.2. Components coupling

The mass transfer is verified using a third test case. A single catalyst particle is surrounded by fluid with a terminal velocity, Fig. 3-left. A first-order reaction occurs inside the particle and internal and external mass transfer limitations are negligible. A solid product forms and remains on the particle. The weight gain of the particle can be calculated from equation (37).

$$m_{MGM}(t) = 4\pi r_g^2 \cdot N_g \cdot k_{reaction} \cdot M_{bulk} \cdot MW_{prod} \cdot t \tag{37}$$

where r_g is the grain radius, N_g is the number of grains in the MGM model, $k_{reaction}$ is the surface reaction rate, M_{bulk} is the concentration of the reactant in the bulk of the gas, MW_{prod} is the molar weight of the formed solid, and t is time. Fig. 6 compares the simulation results with the analytical solution and verifies the implementation of the mass balance and solid formation.

In order to verify the two-way fluid-particle mass transfer, a packed bed of 31250 ($25\times25\times50$) particles was considered, Fig. 3-right. Three components with different mass transfer coefficients and conditions are considered:

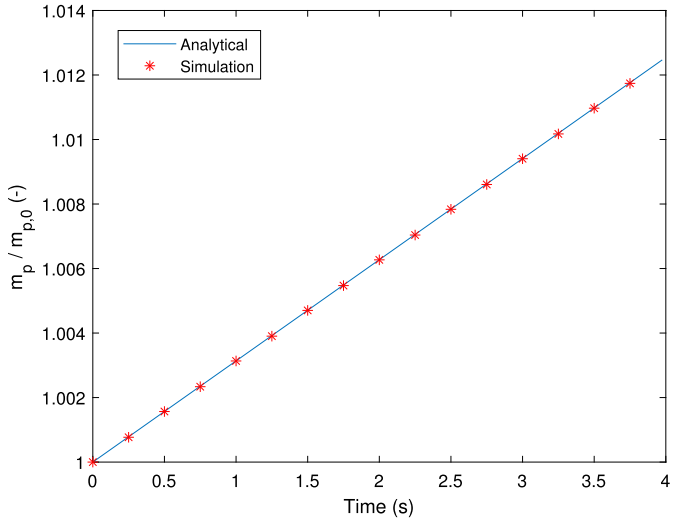

Fig. 6. Comparison of the ratio mass of the particle over time to its initial mass calculated from analytical solution and simulation.

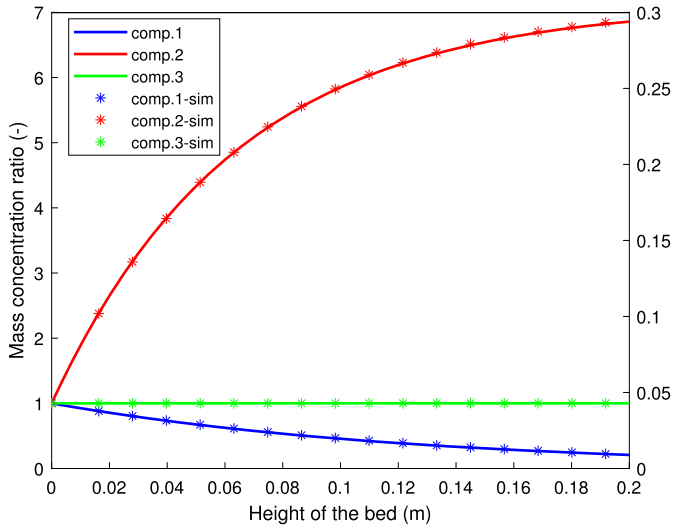

Fig. 7. Comparison of the ratios of concentrations of the components along the height of the bed to the inlet concentrations, obtained from analytical solution and simulation.

- Component-1: no mass transfer between the phases is considered.
- Component-2 has a mass transfer coefficient of 0.005 m/s and component 2 reacts inside the particle with a high reaction rate.
- Component-3 has a mass transfer coefficient of 0.01 m/s and has a constant concentration inside the particle (0.1 kg/m^3) which is higher than the fluid inlet.

The fluid density and particles' size are constant and the flow velocity is not affected by the added or removed mass (i.e. the fluid is incompressible). In this case, the component concentration along the bed is governed by equation (38):

$$\frac{M_{f,i}(z) - M_{p,i}}{M_{f,i,in} - M_{p,i}} = exp\left(\frac{-k_{m,a,i} a_d z}{u_f}\right) \tag{38}$$

$M_{f,i,in}$ represents the inlet condition. a_d is the exchanging surface area per unit length of the bed, and z is the position along the height of the packed bed. Fig. 7 shows that the analytical and simulation results are in good agreement, and therefore, the implementation is verified. Table 1 presents the other simulation parameters for both verification cases.

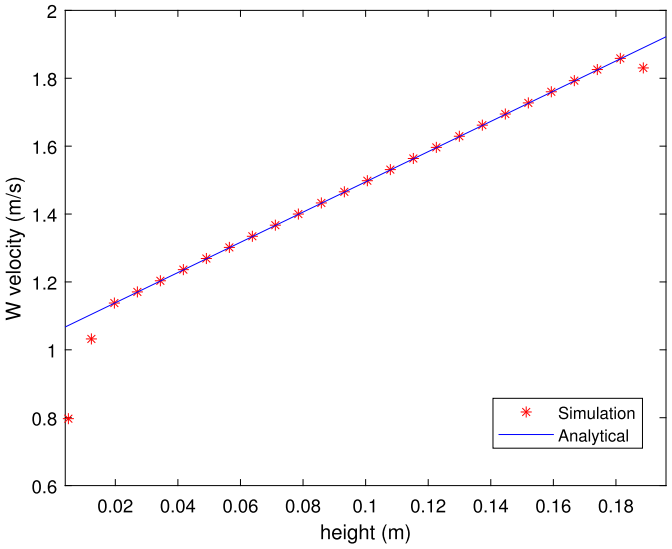

Fig. 8. Comparison of the vertical velocity of the fluid along the height of the bed, obtained from analytical solution and simulation.

3.3. Added/removed mass to/from the gas phase

The removed (or added) mass from/to the fluid phase will affect the fluid phase flow rate and physical properties. A packed bed of 31250 ($25 \times 25 \times 50$) particles is assumed in a fluid with a constant density to verify this effect. Each particle adds a constant source term of $\Psi = 3 \times 10^{-8}\ kg/s$ to the fluid. As a consequence, the fluid velocity along the bed can be calculated with equation (39):

$$u_f(z) = u_f(0) + \frac{\Psi n_p}{\rho_f \varepsilon_f A_c} z \tag{39}$$

where n_p is the number of particles in the unit height of the packed bed, and A_c is the cross-sectional area of the bed. Fig. 8 compares the analytical solution and simulation results and verifies the correct implementation of the model. The deviation at the inlet and outlet is due to the change in porosity because of the begin and end position of the packing.

3.4. Integral mass balance of the reactor

In order to verify the conservation of mass along the reactor, a column with dimensions of $0.1\ m \times 0.1\ m \times 0.5\ m$ was considered with 800 fixed particles at the height of 0.1 m. A constant feed of 70 vol.% inert and 15 vol.% of each reactant and product is introduced. The flux of each component entering and leaving the column is calculated. In the case of a product and reactant containing similar molar weights, the ratio of the gain in the mass of the product to the loss of the mass of the reactant should match the reaction stoichiometry. This factor was evaluated with different reaction stoichiometric ratios and the error was always below 0.03%.

4. Results and discussion

4.1. Case description

In order to demonstrate the capability of the newly developed CFD-DEM-MGM model, a fluidized bed reactor of catalyst particles is modeled. An arbitrary equilibrium reaction is chosen to occur inside the catalyst particles, represented by expression (40) and rate equation (41). Table 2 shows the most important settings of the simulation. The particle size increases over time resulting in altered bed hydrodynamics. Secondly, the balance between the mass transfer limitations and evolving catalytic reaction is gradually changing. Fig. 9 shows snapshots of the catalyst particles in the center of the reactor (0.05 m depth) colored according to the radius after 3.5 s (left) and 8 s (right). In the next sections the evolution of these parameters is evaluated in more detail.

Table 2
Simulation settings and properties of the analyzed test case.

Name	Value	Unit
Reactor dimensions (width×depth×height)	$0.1 \times 0.1 \times 1$	m
Field grid size	$20 \times 20 \times 160$	-
Flow time step size	1×10^{-4}	s
Particle time step size	2×10^{-5}	s
Inlet gas velocity	3.5	m/s
Inlet gas temperature	850	K
Inlet gas composition	80 – 15 – 5	vol.%(A – B – inert)
Initial reactor temperature	800	K
Initial reactor composition	5 – 10 – 85	vol.%(A – B – inert)
Number of particles	25000	-
Particles initial diameter	4	mm
Number of grain layers in particles	20	-
Particle density	1309	kg/m^3
Geldart classification type	D	-
Normal restitution coefficient p-p / p-w	0.96 / 0.86	-
Tangential restitution coefficient p-p / p-w	0.33 / 0.33	-
Friction coefficient p-p / p-w	0.15 / 0.15	-

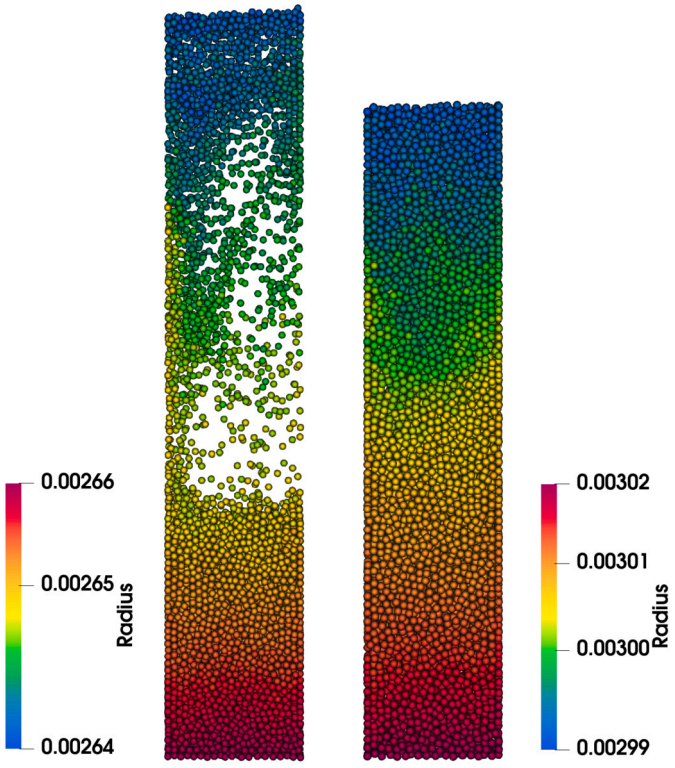

Fig. 9. Illustration of the particles in the center of the reactor (0.02 m depth) colored according to the radius after 3.5 s (left) and 8 s (right).

$$2\mathrm{A(g)} \rightleftharpoons 2\mathrm{B(g)} + \mathrm{C(s)} \qquad \Delta H_{(298K)} = +74.5\,kJ/mol \tag{40}$$

$$-r_A = k\left(P_{CH_4}{}^2 - \frac{P_{H2}{}^2}{K_p}\right) \tag{41}$$

4.2. Particle size growth

As the reaction evolves over time inside the catalyst particles with accompanying solid product formation, the catalyst particle size increases over time. As a result the bed height increases. Fig. 10-left shows that particles grow as the reaction occurs. During the initial phase, there

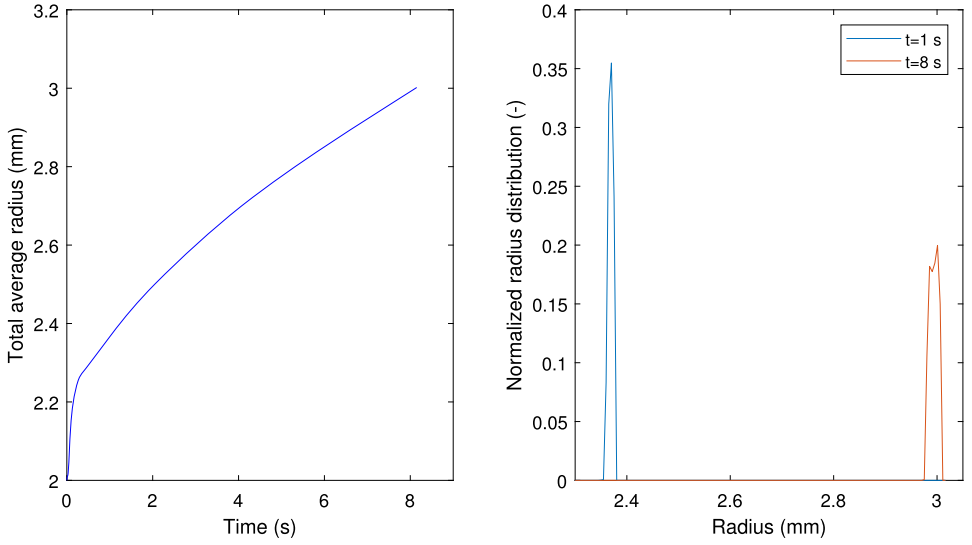

Fig. 10. Left: the average size of all particles in the reactor over time. Right: normalized particle size distribution after 3.5 and 8 seconds of the start of the reaction. The tiny double peak on the red graph is due to classifying particles into size classes when plotting.

is no product layer around the grains and therefore no mass and heat transfer resistance prevails in the grains; therefore, the radius increases at a higher rate compared to a later stage in this process.

Although the particles near the bottom of the reactor are experiencing a higher reaction rate due to the higher reactant concentration and lower product concentration, Fig. 10-right shows that initially, particles grow at a uniform rate due to the intense bed mixing under the influence of vigorous fluidization and therefore the particle size distribution is very narrow. However, as it is mentioned in section 4.3 mixing of particles is reduced over time and, therefore a wider particle size distribution is obtained in the later stages. As it is visible in the snapshots of Fig. 9 there is a gradient of size along the height of the reactor.

4.3. Fluidization regime

Since the larger particles are heavier and require a higher gas velocity in order to remain fluidized, the excess velocity decreases with the associated impact on fluidization characteristics over time. Fig. 11 shows the porosity at the central plane of the bed at different times. The void volume within a macro particle is not considered in calculating reactor porosity. It is obvious that initially bubbles and slugs are formed, however after 6.5 s the bed is completely defluidized whereas the height of the bed has expanded considerably.

Fig. 12 shows the average ratio of the drag force imposed on the particles to the minimum required drag force for the fluidization of the bed (which is the buoyant weight of the particles). Initially, particles descend and accumulate at the bottom of the reactor, causing a reduction in bed porosity. This reduction in porosity induces a high gas velocity, resulting in significant drag force on the particles. Consequently, the particles are propelled upward within the bed, leading to the formation of slugs. The expansion of the bed height caused by slug formation subsequently diminishes the bed porosity, thereby reducing the drag force exerted on the particles. As a consequence, the particles descend once again toward the bottom of the bed, initiating a recurring cycle of particle movement. The reduction in the fluctuations shows that the intensity of bubble formation is reduced until eventually the bed is defluidized. Furthermore, the frequency of the fluctuations is also reduced, confirming the hydrodynamic regime change.

Fig. 13 depicts the solids motion at three different times. Initially particles experience significant vertical movements. Over time the solid mobility is reduced. Eventually the bed is defluidized and the only movement is due to particle growth and consequently the bed height expansion.

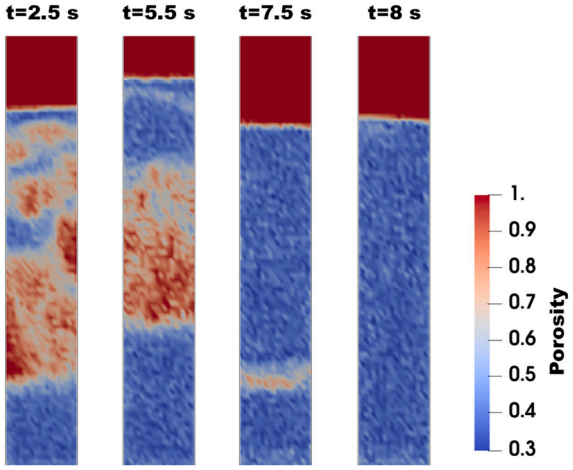

Fig. 11. Snapshots of the porosity at the central sheet of the bed over time.

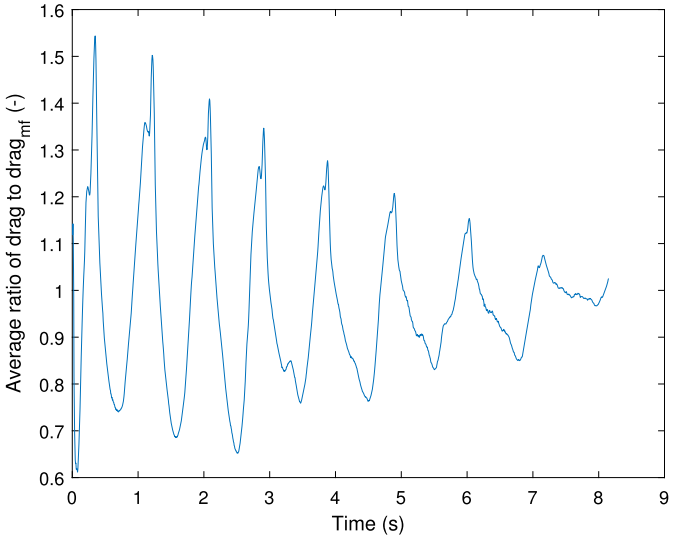

Fig. 12. Average ratio of the drag force on the particles to the minimum required drag force for fluidization of particles.

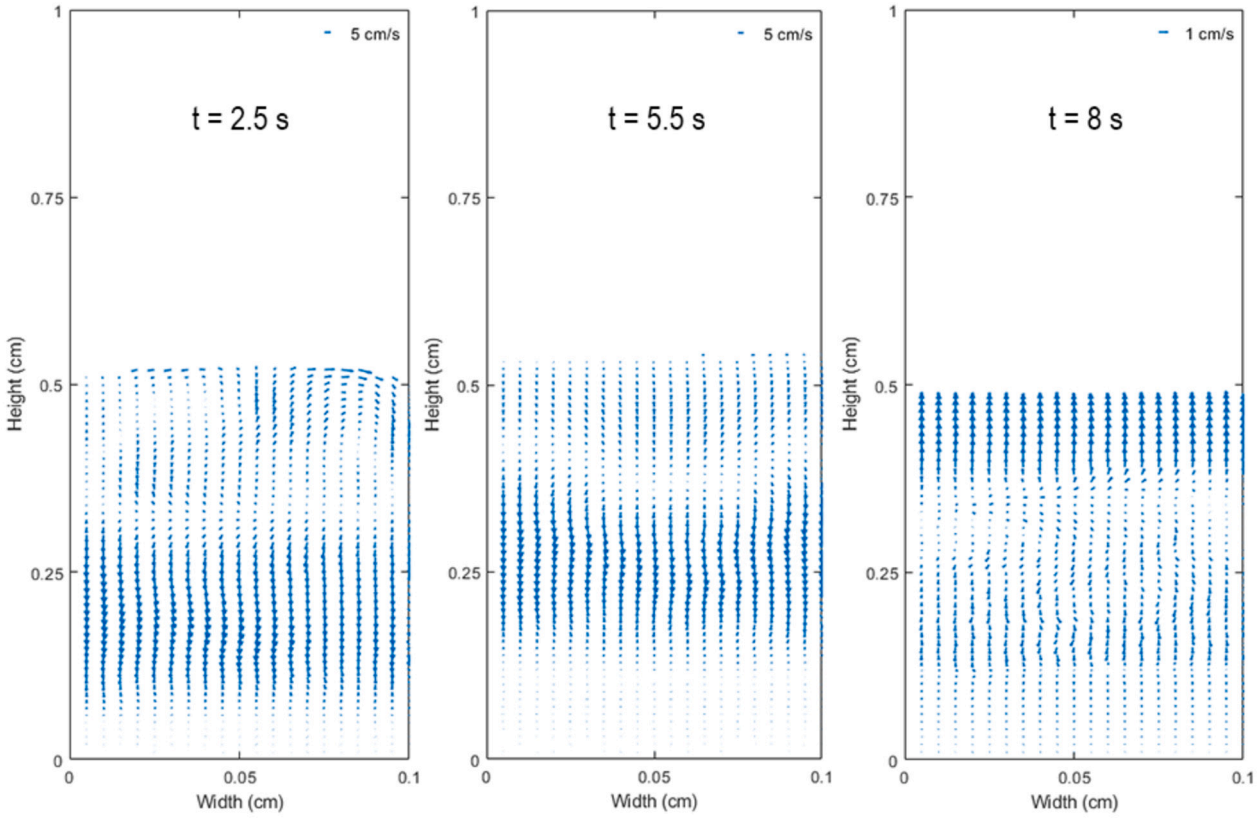

Fig. 13. Instantaneous solids velocity at different times. Please note the scale differences. Over time the solid mobility and mixing are reduced.

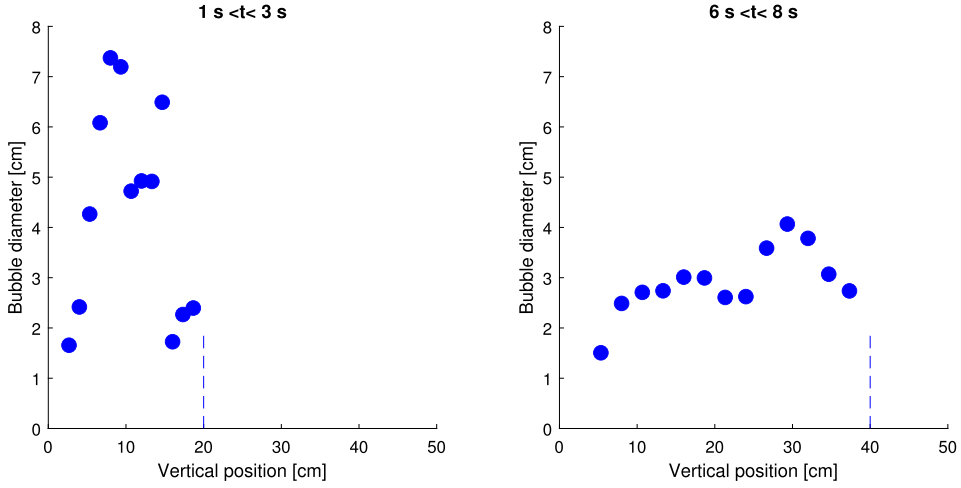

Fig. 14. Average bubble size along the bed height between 1 s< t <3 s (left) and 6 s< t <8 s (right). Dash lines show the cut-off height for bubble detection, and represent the approximate bed height.

Fig. 14-left demonstrates the initial formation of bubbles at the bottom of the reactor, which rapidly transition into slugs as they ascend. Nevertheless, as the slugs reach higher heights within the reactor, the particles situated above them descend and disrupt the slugs, causing them to break into smaller bubbles once again (Fig. 11).

In the later stages of the process, the minimum gas velocity required for fluidization increases. Consequently, the excess gas velocity decreases, resulting in the formation of smaller bubbles (Fig. 14-right), compared to the initial stages. This change in bubble size distribution is attributed to the elevated minimum fluidization velocity, which affects the overall fluidization behavior and the resulting bubble dynamics.

4.4. External and intra-particle mass transfer limitations

If the reaction rate is assumed to be pseudo-first-order as equation (42), then the impact and importance of the fluidization regime and particle size on the performance of the process can be evaluated by the second Damköhler number (Da_{II}). This number represents the ratio of the chemical reaction rate, to the external mass transfer rate, as given by equation (43) (Bird et al., 2001). Where k_m is the mass transfer coefficient calculated from equation (22), while the indices s and $bulk$ refer to surface and local concentrations and temperature.

$$-r'_A\left[\frac{mol}{m^3 . s}\right] = \hat{k}_1\left[\frac{1}{s}\right]C_A\left[\frac{mol}{m^3}\right] \tag{42}$$

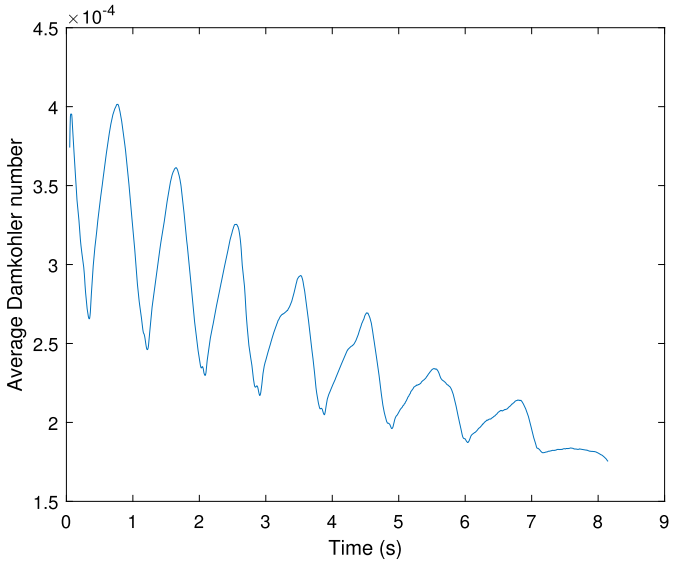

Fig. 15. The average Da_{II} of the particles gradually decreases over time due to particle growth and a lower density of active sites in larger particles. The fluctuations follow the hydrodynamics of the bed.

$$Da_{II} = \frac{R_p \hat{k}_1 C_{A,s}}{3 k_m C_{A,bulk}} \tag{43}$$

To linearize the actual reaction kinetics (as shown in Equation (41)) to first order, a unit conversion is necessary, which is described by Equation (44). Consequently, the rate constant of the pseudo-first-order reaction rate is determined by Equation (45).

$$-r_A[\frac{mol_A}{g_{fresh\,cat}s}] \times 10^3 [\frac{g_{fresh\,cat}}{kg_{fresh\,cat}}] \times \frac{m_0}{V_p}[\frac{kg_{fresh\,cat}}{m^3}] = -r'_A[\frac{mol_A}{m^3\,s}] \tag{44}$$

$$\hat{k}_1 = \frac{-r_A \times \frac{m_0}{V_p} \times 10^3}{C_A} \tag{45}$$

Fig. 15 illustrates the gradual decrease of Da_{II} over time, attributed to the reduction in $\hat{k}_1$ resulting from the declining density of active sites per unit volume of the particle, which is inversely proportional to the third power of R_p. The magnitude of Da_{II} suggests that the influence of external mass transfer limitations on the reaction rate and reactor performance can be considered negligible throughout the entire process duration. By comparing Figs. 12 and 15, it is evident that the Da_{II} closely follows the hydrodynamic behavior and exhibits the same oscillation frequency due to the dependency of the mass transfer coefficient on the relative velocity between the particles and the gas phase.

On the other hand, the increase of particle size and the formation of solid products can alter the diffusional limitations of the process. The assessment of this effect can be accomplished by analyzing the Thiele modulus (ϕ^2), which represents the ratio of the chemical reaction rate to the pore diffusion rate. For the assumed pseudo-first-order reaction rate (equation (42)), the calculation of ϕ^2 is performed using Equation (46) (Bird et al., 2001; Delparish et al., 2023).

$$\phi^2 = R_p^2 \frac{\hat{k}_1}{D^{\text{eff}}} \tag{46}$$

Fig. 16 demonstrates the decreasing trend of ϕ^2 over time, primarily due to the diminishing value of $\hat{k}_1$, which exhibits an inverse relationship with the third power of R_p. Despite the external mass transfer limitation, ϕ^2 emphasizes that diffusional effect cannot be disregarded and its significance may vary throughout the course of the process.

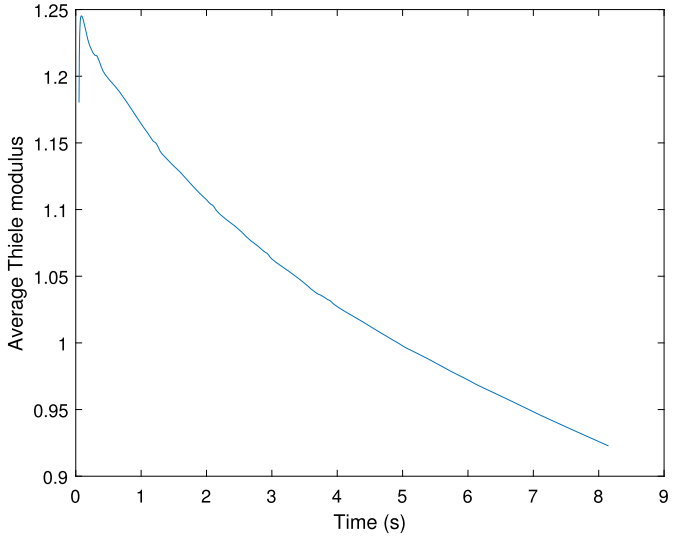

Fig. 16. The average ϕ^2 of the particles decreases over time. The graph highlights that pore diffusion limitations are comparatively as significant as the reaction kinetics for the given pseudo-first-order reaction rate.

5. Conclusions

A CFD-DEM-MGM model for growing catalyst particles inside a reactor has been developed to study particle growth's impact on the bed hydrodynamics and heat and mass transfer rates. The CFD-DEM-MGM was verified in different aspects such as two-way heat and mass transfer by comparing results with trusted analytical solutions. In order to assess the capabilities of the model and evaluate its effectiveness in replicating the dynamic behavior of the reactor system, a simulation was conducted on a fluidized bed reactor consisting of catalyst particles exhibiting an arbitrary reaction.

Initially, the particle size increased uniformly inside the reactor due to good solid mixing. However, the increase of the particle size led to changing fluidizing behavior and a reduced solids mixing rate. Eventually, complete defluidization of the fluidized bed reactor was observed. As a result, a particle size gradient was noted along the height of the reactor.

The presented results indicate that the model is capable of coupling the effects of hydrodynamics in a fluidized bed with reacting and growing particles, incorporating the time-dependent effects of mass and heat transfer. For example, for the chosen arbitrary reaction, it incorporates that the effect of internal mass transfer limitations is slowly becoming important as the particles grow according to the MGM part of the model.

The CFD-DEM-MGM model and the findings of this work can be used for processes such as polymerization or thermocatalytic decomposition of methane where there is a net transfer to or from the catalyst particle due to a gas-solid reaction and where both the external and internal particle properties play an important role in the process performance. This model can be used to gain knowledge to support efficient reactor selection and design and provides a learning model for larger process design.

Declaration of competing interest

The authors declare the following financial interests/personal relationships which may be considered as potential competing interests:

J.A.M. Kuipers reports financial support was provided by Dutch Research Council.

Data availability

Data will be made available on request.

Acknowledgement

This work is part of the Advanced Research Center for Chemical Building Blocks, ARC CBBC, which is co-founded and co-financed by the Netherlands Organisation for Scientific Research (NWO) and the Netherlands Ministry of Economic Affairs.

The authors also acknowledge J.G. Ramírez (Multiphase Reactors Group, Department of Chemical Engineering & Chemistry, Eindhoven University of Technology) for his contribution to the CFD-DEM model, A.P. van Bavel (Shell Global Solutions International B.V.) and B.H. Reesink (BASF Nederland B.V.) for their contributions in the discussions.

References

Tsuji, Y., Kawaguchi, T., Tanaka, T., 1993. Discrete particle simulation of two-dimensional fluidized bed. Powder Technol. (ISSN 0032-5910) 77 (77), 79–87. https://doi.org/10.1016/0032-5910(93)85010-7.

De Jong, J.F., Dang, T.Y.N., Van Sint Annaland, M., Kuipers, J.A.M., 2012. Comparison of a discrete particle model and a two-fluid model to experiments of a fluidized bed with flat membranes. Powder Technol. (ISSN 0032-5910) 230, 93–105. https://doi.org/10.1016/J.POWTEC.2012.06.059.

Golshan, S., Sotudeh-Gharebagh, R., Zarghami, R., Mostoufi, N., Blais, B., Kuipers, J.A.M., 2020. Review and implementation of CFD-DEM applied to chemical process systems. https://doi.org/10.1016/j.ces.2020.115646.

Mu, L., Buist, K.A., Kuipers, J.A.M., Deen, N.G., 2020. Scaling method of CFD-DEM simulations for gas-solid flows in risers. Chem. Eng. Sci., X (ISSN 2590-1400) 6, 100054. https://doi.org/10.1016/J.CESX.2019.100054.

Norouzi, H.R., Zarghami, R., Sotudeh-Gharebagh, R., Mostoufi, N., 2016. Coupled CFD-DEM Modeling: Formulation, Implementation and Application to Multiphase Flows. John Wiley & Sons. ISBN 9781119005315.

Finotello, G., Padding, J.T., Buist, K.A., Schijve, A., Jongsma, A., Innings, F., Kuipers, J.A.M., 2019. Numerical investigation of droplet-droplet collisions in a water and milk spray with coupled heat and mass transfer. Dry. Technol. 38 (12), 1597–1619. https://doi.org/10.1080/07373937.2019.1651732. ISSN 15322300.

Zhuang, Y.Q., Chen, X.M., Luo, Z.H., Xiao, J., 2014. CFD–DEM modeling of gas–solid flow and catalytic MTO reaction in a fluidized bed reactor. Comput. Chem. Eng. (ISSN 0098-1354) 60, 1–16. https://doi.org/10.1016/J.COMPCHEMENG.2013.08.007.

Lu, L., Gao, X., Shahnam, M., Rogers, W.A., 2020. Bridging particle and reactor scales in the simulation of biomass fast pyrolysis by coupling particle resolved simulation and coarse grained CFD-DEM. Chem. Eng. Sci. (ISSN 0009-2509) 216, 115471. https://doi.org/10.1016/J.CES.2020.115471.

Wang, J., Ku, X., Yang, S., 2022. Simulation of biomass pyrolysis in a rotary drum by coupling CFD-DEM with a one-dimensional thermally thick model. Energy Fuels (ISSN 0887-0624) 36 (7), 3665–3679. https://doi.org/10.1021/ACS.ENERGYFUELS.2C00050.

Oyedeji, O.A., Brennan Pecha, M., Finney, C.E., Peterson, C.A., Smith, R.G., Mills, Z.G., Gao, X., Shahnam, M., Rogers, W.A., Ciesielski, P.N., Brown, R.C., Parks, J.E., 2022. CFD–DEM modeling of autothermal pyrolysis of corn stover with a coupled particle- and reactor-scale framework. Chem. Eng. J. (ISSN 1385-8947) 446, 136920. https://doi.org/10.1016/J.CEJ.2022.136920.

Pecha, M.B., Thornburg, N.E., Peterson, C.A., Crowley, M.F., Gao, X., Lu, L., Wiggins, G., Brown, R.C., Ciesielski, P.N., 2021. Impacts of anisotropic porosity on heat transfer and off-gassing during biomass pyrolysis. Energy Fuels 35 (24), 20131–20141. https://doi.org/10.1021/ACS.ENERGYFUELS.1C02679/ASSET/IMAGES/LARGE/EF1C02679_0008.JPEG. ISSN 15205029.

Lu, L., Gao, X., Shahnam, M., Rogers, W.A., 2021. Simulations of biomass pyrolysis using glued-sphere CFD-DEM with 3-D intra-particle models. Chem. Eng. J. (ISSN 1385-8947) 419, 129564. https://doi.org/10.1016/J.CEJ.2021.129564.

Hadian, M., Buist, K.A., Bos, A.N.R., Kuipers, J.A.M., 2021. Single catalyst particle growth modeling in thermocatalytic decomposition of methane. Chem. Eng. J. 421, 129759. https://doi.org/10.1016/j.cej.2021.129759. ISSN 13858947.

Chiovetta, M.G., Estenoz, D.A., 2004. Behavior of active sites in a changing, supported metallocene catalyst particle: modeling monomer transport and kinetics. Macromol. Mater. Eng. (ISSN 1438-7492) 289 (11), 1012–1026. https://doi.org/10.1002/mame.200400069.

McKenna, T.F., Soares, J.B., 2001. Single particle modelling for olefin polymerization on supported catalysts: a review and proposals for future developments. Chem. Eng. Sci. 56 (13), 3931–3949. https://doi.org/10.1016/S0009-2509(01)00069-0. ISSN 00092509.

Li, Z., Janssen, T.C.E., Buist, K.A., Deen, N.G., van Sint Annaland, M., Kuipers, J.A.M., 2017. Experimental and simulation study of heat transfer in fluidized beds with heat production. Chem. Eng. J. (ISSN 1385-8947) 317, 242–257. https://doi.org/10.1016/J.CEJ.2017.02.055.

Anderson, J.D., Wendt, J., 1995. Computational Fluid Dynamics, vol. 206. Springer.

Patil, A.V., Peters, E.A.J.F., Kuipers, J.A.M., 2015. Comparison of CFD-DEM heat transfer simulations with infrared/visual measurements. Chem. Eng. J. 277, 388–401. https://doi.org/10.1016/j.cej.2015.04.131. ISSN 13858947.

Sarkar, S., van der Hoef, M.A., Kuipers, J.A.M., 2009. Fluid-particle interaction from lattice Boltzmann simulations for flow through polydisperse random arrays of spheres. Chem. Eng. Sci. 64 (11), 2683–2691. https://doi.org/10.1016/j.ces.2009.02.045. ISSN 00092509.

Beetstra, R., Van Der Hoef, M.A., Kuipers, J.A.M., 2007. Drag force of intermediate Reynolds number flow past mono- and bidisperse arrays of spheres. AIChE J. 53 (2), 489–501. https://doi.org/10.1002/aic.11065. ISSN 15475905.

Hoomans, B.P.B., Kuipers, J.A.M., Briels, W.J., Van Swaaij, W.P.M., 1996. Discrete particle simulation of bubble and slug formation in a two-dimensional gas-fluidised bed: a hard-sphere approach. Chem. Eng. Sci. 51 (1), 99–118. https://doi.org/10.1016/0009-2509(95)00271-5. ISSN 00092509.

Wendt, J.F., Anderson, J.D., Degroote, J., Degrez, G., Dick, E., Grundmann, R., Vierendeels, J., 2009. Computational Fluid Dynamics: An Introduction, pp. 1–332.

Cundall, P.A., Strack, O.D., 1979. A discrete numerical model for granular assemblies. Geotechnique 29 (1), 47–65. https://doi.org/10.1680/GEOT.1979.29.1.47. ISSN 17517656.

Buist, K.A., Seelen, L.J.H., Deen, N.G., Padding, J.T., Kuipers, J.A.M., 2016. On an efficient hybrid soft and hard sphere collision integration scheme for DEM. Chem. Eng. Sci. (ISSN 0009-2509) 153, 363–373. https://doi.org/10.1016/J.CES.2016.07.030.

Kloss, C., Christoph, G., Hager, A., Amberger, S., Pirker, S., 2012. Models, algorithms and validation for opensource DEM and CFD-DEM. Prog. Comput. Fluid Dyn. 12, 140–152.

Gunn, D.J., 1978. Transfer of heat or mass to particles in fixed and fluidised beds. Int. J. Heat Mass Transf. (ISSN 0017-9310) 21 (4), 467–476. https://doi.org/10.1016/0017-9310(78)90080-7.

Anzelius, A., 1926. Über erwärmung vermittels durchströmender medien. J. Appl. Math. Mech. (Z. Angew. Math. Mech.) (ISSN 0044-2267) 6 (4), 291–294.

Bateman, H., 1932. Partial Differential Equations of Mathematical Physics.

Hougen, O.A., Watson, K.M., Ragatz, R.A., 1947. Chemical Process Principles. 3. Kinetics and Catalysis. Wiley.

Bird, R.B., Stewart, W.E., Lightfoot, E.N., 2001. Transport Phenomena, 2nd edition. John Wiley & Sons, New York.

Delparish, A., de Leeuw den Bouter, W.N., Yercan, A., van der Schaaf, J., Fernanda Neira d'Angelo, M., 2023. Bringing the promises of microreactors and gold catalysis to lignocellulosic biomass valorization: a study on oxidative transformation of furfural. Chem. Eng. J. (ISSN 1385-8947) 452, 138903. https://doi.org/10.1016/J.CEJ.2022.138903.